

1 Causal and uncertainty-aware digital-twin framework for ultra-low-noise geoscientific inertial sensors

2

3

4 Antonino D'Alessandro

5 Istituto Nazionale di Geofisica e Vulcanologia, Osservatorio Nazionale, Rome, Italy

6 antonino.dalessandro@ingv.it

7

8

9 Abstract

10 Ultra-low-noise inertial sensors are a cornerstone of modern geoscientific instrumentation, enabling high-
11 resolution observations across seismology, geodesy, gravimetry, and vibration isolation. Achieving and reliably
12 predicting their performance requires a rigorous treatment of physical causality, noise propagation, and
13 uncertainty, particularly in force-feedback architectures operating near fundamental limits. In this study, we
14 introduce a causal and uncertainty-aware digital-twin framework for the design and metrological assessment
15 of ultra-low-noise geoscientific inertial sensors. The proposed framework integrates mechanical dynamics,
16 force-feedback control, transduction, and digital acquisition within a physically realisable model that explicitly
17 enforces causality and stability constraints. Starting from a minimal equation-of-motion description, the digital
18 twin is formulated in the frequency domain to construct causal transfer functions and a comprehensive noise-
19 budget model. The framework enables the systematic separation of fundamental thermal noise limits from
20 implementation-dependent noise sources, including readout, actuation, and digital acquisition effects. We
21 introduce quantitative performance metrics based on self-noise spectra, dominant noise regimes, crossover
22 frequencies, and near-plateau bandwidths, allowing complex spectral behaviour to be condensed into
23 actionable design indicators. Parameter uncertainties are propagated through the digital twin to provide
24 uncertainty-aware performance estimates and robustness diagnostics. Through a series of illustrative analyses,
25 we demonstrate how the proposed digital twin supports informed design trade-offs, identifies performance
26 bottlenecks, and prevents non-physical or overly optimistic sensitivity estimates arising from non-causal
27 modelling assumptions. While focused on inertial sensors, the methodology is general and transferable to other

28 classes of geoscientific instruments. The framework provides a transparent and extensible foundation for next-
29 generation sensor design, virtual experimentation, and metrologically consistent performance prediction.

30

31

32 **1. Introduction**

33 The design and metrological assessment of ultra-low-noise inertial sensors for geoscientific applications
34 remains a central challenge in measurement science and engineering. These sensors — including broadband
35 seismometers, compact accelerometers, and advanced gravimetric devices (Prasad et al., 2022) — are critical
36 for resolving weak ground motions across broad frequency bands, enabling high-precision environmental
37 monitoring, earthquake early warning, and advanced observational geodesy. In practice, instrument
38 performance is constrained by a combination of fundamental thermomechanical limits and implementation-
39 dependent noise sources such as thermal (Brownian) noise of mechanical suspensions, readout electronics
40 noise, quantization error in digital acquisition, and control-loop artefacts (Ubhi et al., 2022; Zhao et al., 2022;
41 van Dongen et al., 2023).

42 Traditional sensor development has often proceeded through incremental improvements of individual
43 components, with performance characterised post-facto via laboratory calibration and field testing. While such
44 approaches are effective for benchmarking specific prototypes, they provide limited insight into the system-
45 level trade-offs between sensitivity, bandwidth, dynamic range, and robustness, particularly when uncertainty
46 propagation across the entire measurement chain is of interest. The need for rigorous uncertainty frameworks
47 in sensor design is well recognised in inertial navigation and metrology communities, where stochastic error
48 modelling and error budgeting have been emphasised (El-Sheimy et al., 2020).

49 In parallel, the concept of a digital twin has emerged as a powerful paradigm for unifying physics-based
50 simulation with real-time measurement data, enabling advanced prediction, optimisation, and uncertainty
51 quantification in complex engineered systems. Digital twin methodologies have been extensively reviewed in
52 industrial and infrastructure domains, highlighting their potential for model-based monitoring and decision
53 support (Sun et al., 2024; Carlin et al., 2024). **Recent developments have increasingly focused on uncertainty-
54 aware and physics-informed digital twins for metrological applications, with particular emphasis on
55 traceability, virtual experimentation, and hybrid modelling approaches that combine physical models with**

56 data-driven components (e.g., Wright and Davidson, 2024; Maculotti et al., 2024; Sun et al., 2024). In
57 metrology, digital twins are gaining traction as tools for virtual calibration, uncertainty evaluation, and
58 traceability analysis across diverse measurement systems, including coordinate measuring machines, optical
59 scanners, and virtual metrological experiments (Vlaeyen et al., 2021; Poroskun et al., 2022).

60 Despite these advances, the digital-twin literature remains fragmented with respect to sensor-centric, causal,
61 and uncertainty-aware frameworks that encompass both physical dynamics and digital acquisition processes.
62 Many digital twin formulations in metrology still focus on high-level concepts or specific subsystems, without
63 enforcing physical causality and realisability constraints essential for accurate modeling of closed-loop, force-
64 feedback inertial sensors. Furthermore, the representation and propagation of uncertainty through the digital
65 twin's internal variables and across the physical–digital boundary is often treated qualitatively or post hoc
66 rather than systematically (Ríos et al., 2020).

67 In the field of inertial sensing, contemporary research continues to push performance boundaries through
68 innovative mechanics and novel readout schemes, such as interferometric sensing with enhanced dynamic
69 range and low noise floors (Kranzhoff et al., 2023), as well as advanced tilt and vibration measurement systems
70 that delineate thermal and readout noise dominance across frequency (Bai et al., 2025). In particular, recent
71 work has demonstrated significant progress in ultra-low-noise interferometric readout systems and compact
72 inertial sensor architectures, pushing noise floors closer to fundamental limits while maintaining practical
73 deployability (Carter et al., 2024; Carter et al., 2025; Bai et al., 2025). These efforts underscore the importance
74 of integrated noise budgeting and uncertainty analysis, yet a comprehensive, unified framework that couples
75 physical system dynamics, sensor signal chains, and digital data acquisition with rigorous uncertainty
76 propagation is still absent.

77 This manuscript addresses these gaps by introducing a causal and uncertainty-aware digital-twin framework
78 for ultra-low-noise geoscientific inertial sensors. The framework enforces physical causality and realisability
79 constraints while systematically propagating uncertainty from mechanical parameters and control elements
80 through to spectral performance metrics. It integrates mechanical modelling, transduction chains, force-
81 feedback architectures, and digital acquisition within a single, physically consistent representation (Fig. 1). By
82 decomposing self-noise into fundamental and implementation-dependent contributions and identifying

83 dominant noise regimes, the framework facilitates quantitative evaluation of design choices and metrological
84 limits.

85 Rather than relying on experimental datasets, the methodology is conceived as a design-stage tool to guide
86 sensor architecture choices and parameter selection prior to hardware realisation. The remainder of this paper
87 is organised as follows: Section 2 formalises design requirements and problem scope; Section 3 presents the
88 digital-twin architecture; Section 4 develops the comprehensive noise model; Sections 5 and 6 analyse spectral
89 performance and design trade-offs; Section 7 synthesises performance metrics and optimisation strategies;
90 Section 8 discusses broader implications and limitations; and Section 9 concludes with final remarks.

91

92

93 **2. Design requirements and problem formulation**

94 The design of ultra-low-noise inertial sensors for geoscientific applications constitutes a multi-objective
95 optimisation problem in which sensitivity, bandwidth, dynamic range, robustness, and practical
96 implementation constraints must be addressed simultaneously. Unlike post-deployment performance
97 assessment or component-level optimisation approaches, the present study formulates the sensor design
98 problem explicitly at the pre-implementation stage, adopting a system-level perspective aimed at predicting
99 achievable performance prior to hardware realisation.

100 The conceptual scope of the problem is illustrated in Fig. 1, which summarises the functional elements of a
101 force-feedback inertial sensor and their interactions. Within this framework, design requirements are not
102 treated as independent specifications but as coupled constraints that jointly define the admissible design space.

103 The primary requirement considered in this work is the attainment of ultra-low self-noise levels over a broad
104 frequency band spanning the ultra-low-frequency (ULF) regime to the classical broadband (BB) seismic band.
105 Such performance is essential for a wide range of geoscientific applications, including broadband seismology,
106 gravimetry, and long-term environmental monitoring, where weak ground motions must be resolved across
107 several decades in frequency (Collette et al., 2012; Carter et al., 2024).

108 A second key requirement concerns dynamic range and saturation behaviour. Ultra-low-noise operation must
109 coexist with the capability to accommodate large transient signals without loss of linearity, control stability, or
110 actuator authority (Sider et al., 2023). In force-feedback architectures, this requirement couples mechanical

111 design parameters, actuation strength, and control loop characteristics, precluding their independent
112 optimisation (Zhao et al., 2022).

113 Additional constraints arise from digital acquisition and system-level resources, including power consumption,
114 telemetry bandwidth, and data resolution. Finite analog-to-digital converter (ADC) resolution, clock jitter, and
115 digital signal processing limitations introduce noise contributions that may dominate the self-noise spectrum
116 over specific frequency ranges, particularly at higher frequencies. These effects must therefore be incorporated
117 explicitly into the design formulation rather than treated as secondary implementation details (El-Sheimy et
118 al., 2020; Ubezio et al., 2023).

119 Finally, the design requirements implicitly assume a set of environmental and operational conditions, including
120 mechanical coupling to the ground, thermal stability, and station infrastructure. While these factors are not
121 modelled explicitly in the present framework, they define the operating context within which the sensor is
122 expected to meet its performance objectives and delimit the interpretation of the resulting performance bounds.
123 On the basis of the above requirements, the design problem is formulated as follows: given a target sensitivity
124 spectrum, a frequency band of interest, and a set of implementation constraints, determine whether a physically
125 realisable inertial sensor architecture can achieve the desired performance and identify the dominant
126 mechanisms limiting that performance.

127 A central aspect of this formulation is the explicit separation between fundamental physical limits, such as
128 thermal noise associated with mechanical dissipation, and implementation-dependent limits arising from
129 readout electronics, actuation mechanisms, feedback control, and digital acquisition. This distinction is
130 essential for meaningful interpretation of noise budgets and for guiding design decisions toward genuinely
131 performance-limiting components rather than secondary contributors (Collette et al., 2012; Maculotti et al.,
132 2024).

133 The sensor is modelled as a linear, time-invariant system operating around a stable equilibrium point. Its
134 behaviour is described through transfer functions linking ground acceleration to the measured output quantity.
135 Nonlinear effects such as actuator saturation, hysteresis, and large-amplitude geometric nonlinearities are
136 neglected. These assumptions are standard in the analysis of ultra-low-noise inertial sensors and are justified
137 when the focus is on noise-limited performance under nominal operating conditions (Carter et al., 2024).

138 Within this framework, the observable of interest is the output acceleration estimate, whose power spectral
139 density is determined by the combined effect of the sensor dynamics and all internal noise sources propagated
140 through the system. The design objective is therefore the optimisation of the total self-noise spectrum, subject
141 to causality, stability, and realisability constraints, rather than the minimisation of individual noise sources in
142 isolation.

143 The formulation adopted here deliberately excludes experimental calibration data and site-specific noise
144 conditions. This choice reflects the intended role of the framework as a design-stage and feasibility-assessment
145 tool, rather than as a post-deployment diagnostic method. While this limits direct comparison with specific
146 instruments, it enables the identification of general trends, trade-offs, and performance bounds that are
147 transferable across sensor classes and deployment scenarios (Wright and Davidson, 2024; Ríos et al., 2020).

148 Model parameters, including mechanical damping and electronic noise levels, are assumed to be characterised
149 by probability distributions reflecting their uncertainty. The systematic propagation of these uncertainties
150 through the digital-twin framework is addressed in subsequent sections. The implications of these assumptions,
151 and their potential impact on real-world performance, are discussed in Section 8.

152

153

154 **3. Digital-twin architecture and causal modeling**

155 The digital twin developed in this study is conceived as a physics-based, causal, and uncertainty-aware
156 representation of an ultra-low-noise inertial sensor, explicitly designed to support metrological analysis and
157 design-stage optimisation. Unlike generic simulation models or reduced-order representations, the proposed
158 digital twin integrates mechanical dynamics, transduction, actuation, control, and digital acquisition within a
159 unified framework that preserves physical causality and realisability.

160 *A frequency-domain representation of the digital-twin response is shown in Fig. 2, illustrating the effect of*
161 *force-feedback control on the system dynamics.* This architecture reflects the functional decomposition of a
162 force-feedback inertial sensor and provides the basis for subsequent noise propagation and performance
163 analysis. *In particular, Fig. 2(a) compares the open-loop mechanical response with the closed-loop response*
164 *obtained under force-feedback control. The open-loop configuration exhibits a pronounced resonance at the*
165 *natural frequency, whereas the closed-loop system suppresses this resonance and reduces proof-mass motion*

166 over a broad frequency band. Fig. 2(b) shows the corresponding force-balance transfer function, highlighting
167 how the feedback force tracks the inertial force at low frequencies and progressively rolls off at higher
168 frequencies due to the finite bandwidth of the control loop.

169 The mechanical subsystem is modelled as a single-degree-of-freedom inertial plant characterised by an
170 effective mass, elastic stiffness, and dissipative damping. This representation captures the dominant dynamics
171 governing the sensor response in the frequency range of interest and is commonly adopted in the analysis of
172 broadband and ultra-low-noise inertial sensors (Collette et al., 2012; Carter et al., 2024).

173 The validity of the single-degree-of-freedom (SDOF) approximation is restricted to the frequency range in
174 which the fundamental mode dominates the mechanical response. In practice, this corresponds to frequencies
175 sufficiently below the first higher-order structural resonance of the sensor assembly, where multi-mode effects
176 and internal deformation of the mechanical structure can be neglected (Collette et al., 2012).

177 At very low frequencies, additional effects such as tilt coupling, foundation compliance, and environmental
178 interactions may introduce deviations from the idealised inertial response. These effects are not explicitly
179 modelled in the present framework and therefore delimit the lower bound of applicability of the SDOF
180 representation.

181 The model further assumes rigid coupling between the sensor frame and the ground, negligible rotational
182 degrees of freedom, and operation in the linear regime around a stable equilibrium configuration. Under these
183 conditions, the SDOF approximation provides an accurate and physically consistent description of the
184 dominant sensor dynamics relevant for noise-limited performance analysis.

185 Thermal noise associated with mechanical dissipation is treated as an intrinsic property of the plant and
186 constitutes a fundamental performance limit. The mechanical model is assumed to operate in the linear regime
187 around a stable equilibrium point, and temperature is treated as a stationary parameter. Spatially distributed
188 modes, geometric nonlinearities, and thermoelastic coupling effects are neglected, an assumption justified
189 when focusing on noise-limited performance well below structural resonance frequencies.

190 The transduction stage converts the mechanical state of the plant into an electrical signal. The digital twin
191 represents this stage through a linear gain and an additive readout noise term, which may encompass optical,
192 capacitive, or electromagnetic sensing mechanisms depending on the sensor implementation. This abstraction
193 allows the framework to remain agnostic with respect to the specific readout technology while retaining its

194 metrological relevance. Compact interferometric readout implementations have recently been integrated in
195 suspended interferometers, providing practical benchmarks for low-noise readout assumptions (Carter et al.,
196 2025; Mitchell et al., 2025).

197 Readout noise is explicitly modelled as a stochastic process whose spectral characteristics can be prescribed
198 or parameterised based on design assumptions. **This representation is consistent with recent advances in ultra-**
199 **low-noise front-end electronics for inertial sensors, where circuit-level optimisation plays a critical role in**
200 **approaching fundamental sensitivity limits (Chen et al., 2024).** This approach is consistent with modern inertial
201 sensor analyses, where readout noise often dominates the self-noise spectrum outside the thermal-noise-limited
202 band (Zhao et al., 2022; Carter et al., 2024).

203 Force-feedback actuation is incorporated into the digital twin to stabilise the mechanical plant and to linearise
204 the sensor response. The actuation subsystem is represented by a causal transfer function linking the control
205 signal to an applied force on the mechanical mass. Actuator noise and finite authority are treated as
206 implementation-dependent limitations and are included explicitly in the model.

207 The control architecture is described by a stabilising controller acting on the measured output. Particular care
208 is taken to ensure that the closed-loop system satisfies causality and stability constraints, as these conditions
209 directly influence noise propagation and achievable performance. Non-causal inversions or idealised feedback
210 laws are deliberately avoided, in contrast to some **analytical treatments that neglect realisability constraints,**
211 **often relying on idealised or non-causal representations of system transfer functions (Oppenheim and Schaffer,**
212 **2010; Bendat and Piersol, 2010).**

213 The final stage of the digital twin represents the digital acquisition process, including analog-to-digital
214 conversion, finite resolution, and timing uncertainty. Quantisation noise and clock jitter are modelled explicitly
215 and propagated through the system in subsequent analyses. This treatment reflects the growing recognition
216 that digital acquisition can impose dominant performance limits in ultra-low-noise sensors, particularly at
217 higher frequencies or under stringent power constraints (El-Sheimy et al., 2020; Ubezio et al., 2023).

218 Discretisation effects are treated consistently with the causal structure of the system. Continuous-time transfer
219 functions are mapped to their discrete-time counterparts using stable and physically meaningful
220 transformations. This ensures that the digital twin remains a faithful representation of a realisable sensor
221 system rather than an idealised mathematical construct. Open-source simulation toolchains widely used in

222 precision interferometry provide a reproducibility baseline for digital-twin implementations (Brown et al.,
223 2020).

224 All model parameters within the digital twin are assumed to be affected by uncertainty arising from
225 manufacturing tolerances, environmental variability, and modelling approximations. These uncertainties are
226 represented through probability distributions assigned to the relevant parameters and are propagated through
227 the digital twin in subsequent sections.

228 It is assumed that parameter uncertainties are statistically independent unless otherwise stated. While this
229 assumption may not hold in all practical cases, it provides a tractable starting point for uncertainty propagation
230 and is consistent with existing metrological digital-twin frameworks (Wright and Davidson, 2024; Maculotti
231 et al., 2024). The implications of this assumption are discussed in Section 8.

232 Within the proposed digital-twin framework, the mechanical plant and the force-feedback actuation are
233 compactly described by the equation of motion

234

$$236 \quad m \ddot{x}(t) + c \dot{x}(t) + k x(t) = - m a_g(t) + F_{fb}(t), \quad (1)$$

235

237 where $x(t)$ denotes the relative displacement of the inertial mass with respect to the sensor frame, $a_g(t)$ is the
238 ground acceleration to be measured (in Fig. 1, the same quantity is represented using the kinematic notation
239 \ddot{u}), m , c , and k represent the effective mass, damping coefficient, and stiffness of the mechanical plant, and
240 $F_{fb}(t)$ is the feedback force applied by the actuator. Equation (1) provides the physical backbone of the digital
241 twin, from which the causal transfer functions and noise propagation relationships are derived in the frequency
242 domain in the following section.

243

244

245 **4. Metrological noise modeling and uncertainty propagation**

246 The metrological performance of an ultra-low-noise inertial sensor is ultimately determined by the propagation
247 of multiple stochastic noise sources through the causal dynamics of the sensor system. Building on the physical
248 model introduced in Section 3, this section formalises the noise modeling framework adopted in the digital

249 twin and defines the methodology used to propagate uncertainty from individual noise sources to the total self-
250 noise spectrum.

251 A schematic overview of the noise budget and its decomposition into individual contributions is shown in Fig.
252 3, which provides a graphical representation of the formalism developed below.

253 Starting from the equation of motion introduced in Eq. (1), the system is transformed into the frequency domain
254 under the assumption of linear, time-invariant dynamics. Taking the Fourier transform of Eq. (1) and using the
255 standard correspondence $d/dt \rightarrow i\omega$, the equation of motion can be written in the frequency domain as

$$256 \quad (-m\omega^2 + ic\omega + k) X(\omega) = -m A_g(\omega) + F_{fb}(\omega),$$

257
258 Denoting Fourier-transformed quantities by capital letters, the relative displacement $X(\omega)$ of the inertial mass
259 can be written as

$$260 \quad X(\omega) = \frac{-m A_g(\omega) + F_{fb}(\omega)}{k - m\omega^2 + ic\omega}, \quad (2)$$

261
262 where $A_g(\omega)$ is the ground acceleration spectrum and $F_{fb}(\omega)$ represents the feedback force in the frequency
263 domain. Equation (2) defines the mechanical susceptibility of the plant and provides the basis for constructing
264 the transfer functions linking each noise source to the sensor output.

265 In a force-feedback configuration, the measured output is typically proportional to an estimate of the ground
266 acceleration derived from the control signal and the plant response. The digital twin represents this relationship
267 through a set of causal transfer functions $T_q(\omega)$, each associated with a specific noise source q .

270 The total self-noise of the sensor is defined as the output noise spectrum obtained in the absence of ground
271 motion, i.e. for $A_g(\omega) = 0$. **Under the assumption of linearity and mutual incoherence of the noise sources,**
272 **the total output power spectral density can be expressed as the sum of the individual contributions propagated**
273 **through their respective transfer functions. This follows from standard results in linear systems theory, where**
274 **each noise source is treated as an independent stochastic input and its contribution is weighted by the squared**
275 **magnitude of the corresponding transfer function (e.g., Bendat and Piersol, 2010; El-Sheimy et al., 2020).**

276 Under this condition, the output acceleration noise power spectral density (PSD) can be expressed as the
277 incoherent sum of the contributions from all internal noise sources,

278

$$280 \quad S_{a,\text{self}}(\omega) = \sum_q |T_q(\omega)|^2 S_q(\omega), \quad (3)$$

279

281 where $S_q(\omega)$ denotes the PSD of the q -th noise source and $T_q(\omega)$ is the corresponding transfer function from
282 that source to the output acceleration estimate. Equation (3) constitutes the central metrological relation of the
283 framework and formalises the noise-budget decomposition illustrated in Fig. 3.

284 The noise sources considered in this work include: (i) thermal (Brownian) noise associated with mechanical
285 dissipation, (ii) readout noise originating from the transduction stage, (iii) actuation noise introduced by the
286 force-feedback mechanism, (iv) digital acquisition noise, including quantisation and timing uncertainty.

287 Thermal noise associated with mechanical damping represents a fundamental physical limit that cannot be
288 reduced without modifying the underlying dissipation mechanisms. Its contribution is governed by the
289 fluctuation–dissipation theorem and depends on temperature, damping, and mechanical susceptibility (Collette
290 et al., 2012).

291 In contrast, readout, actuation, and digital acquisition noises are implementation-dependent and reflect
292 technological and design choices. Their relative importance varies across frequency and design parameter
293 space, and they often dominate the self-noise spectrum outside the thermal-noise-limited band (Zhao et al.,
294 2022; Carter et al., 2024). The explicit separation between these two classes of noise sources is essential for
295 interpreting metrological bounds and guiding effective design optimisation.

296 All noise sources and model parameters entering Eq. (3) are subject to uncertainty arising from manufacturing
297 tolerances, environmental variability, and modelling assumptions. Within the digital-twin framework, these
298 uncertainties are represented through probability distributions assigned to the relevant parameters.

299 Uncertainty propagation is performed by evaluating the statistical distribution of the self-noise spectrum
300 resulting from Eq. (3), given the distributions of $S_q(\omega)$ and the parameters defining $T_q(\omega)$. **This approach is**
301 **consistent with recent developments in digital twin-based uncertainty mapping and error propagation in**
302 **metrological systems, where spatial and parametric uncertainties are explicitly quantified within virtual**

303 representations (Sepahi-Boroujeni and Khameneifar, 2024). This approach enables the estimation of
304 confidence intervals on the predicted self-noise and provides a quantitative measure of robustness with respect
305 to parameter variability, in line with modern metrological digital-twin concepts (Scholz et al., 2022; Wübbeler
306 et al., 2022; Wright and Davidson, 2024; Maculotti et al., 2024).

307 Parameter correlations are neglected unless explicitly stated. While this assumption may not hold in all
308 practical implementations, it allows the identification of dominant uncertainty drivers and represents a
309 reasonable first-order approximation for design-stage analysis.

310 The noise modeling framework assumes linearity, stationarity, and mutual incoherence of the noise sources.
311 Cross-correlations between noise processes and non-stationary effects are not considered. These assumptions
312 are standard in inertial sensor metrology and are justified when the objective is to characterise noise-limited
313 performance under nominal operating conditions.

314 The implications of these assumptions, and their potential impact on real-world sensor behaviour, are discussed
315 in Section 8.

316

317

318 **5. Spectral performance and self-noise regimes**

319 This section analyses the spectral performance predicted by the digital twin and characterises the resulting self-
320 noise in terms of dominant noise regimes across frequency. The objective is to translate the metrological
321 formulation introduced in Section 4 into physically interpretable performance metrics that are directly relevant
322 for sensor design.

323 A representative example of the self-noise spectrum and its decomposition into individual contributions is
324 shown in Fig. 4, which illustrates how fundamental and implementation-dependent noise sources shape the
325 achievable performance across the frequency band of interest.

326 The parameter ranges adopted in this analysis, including mechanical properties, damping ratios, and
327 representative noise levels, are consistent with those reported for state-of-the-art broadband and ultra-low-
328 noise inertial sensors (e.g., Collette et al., 2012; Carter et al., 2024), ensuring that the simulated performance
329 remains representative of physically achievable instrument designs.

330 The total self-noise spectrum $S_{a,\text{self}}(\omega)$, defined in Eq. (3), typically exhibits distinct frequency-dependent
331 behaviours governed by the interplay between mechanical susceptibility and noise transfer functions. Of
332 particular interest is the presence of noise plateaus, i.e. frequency intervals over which the self-noise remains
333 approximately constant.

334 To formalise this concept, the acceleration self-noise amplitude spectral density (ASD) is defined as

335

$$337 \quad N_a(\omega) = \sqrt{S_{a,\text{self}}(\omega)}. \quad (4)$$

336

338 A plateau region is identified when the logarithmic slope of $N_a(\omega)$ with respect to frequency satisfies

339

$$341 \quad \left| \frac{d \log N_a(\omega)}{d \log \omega} \right| < \varepsilon, \quad (5)$$

340

342 where ε is a small threshold chosen to discriminate between flat and sloped spectral behaviour. While the
343 precise value of ε is application-dependent, the qualitative identification of plateau regions is robust with
344 respect to reasonable threshold variations.

345 Plateaus are of particular metrological relevance because they define frequency bands in which the sensor
346 sensitivity is maximised and least sensitive to modelling uncertainties.

347 Across the full frequency band, different noise sources dominate the self-noise spectrum. At low frequencies,
348 the response is typically governed by thermal noise associated with mechanical damping, reflecting the
349 fundamental limit imposed by dissipation mechanisms. In intermediate frequency ranges, readout or actuation
350 noise may dominate, depending on the chosen transduction and control architecture. At higher frequencies,
351 digital acquisition noise, including quantisation and timing uncertainty, often becomes the limiting factor.

352 These dominant noise regimes are identified by comparing the individual terms in Eq. (3) and determining, at
353 each frequency, the noise source contributing the largest fraction to $S_{a,\text{self}}(\omega)$. This regime-based interpretation
354 is illustrated in Fig. 4, where transitions between thermal-limited and implementation-limited behaviour are
355 clearly visible.

356 The identification of dominant regimes is a consolidated result, as it directly follows from the noise budget
357 formalism and does not depend on subjective interpretation. In contrast, the precise frequency boundaries
358 between regimes should be regarded as model-dependent and may shift as design parameters or uncertainty
359 assumptions are varied.

360 A central outcome of the spectral analysis is the explicit comparison between the total self-noise and the
361 thermal noise floor. The ratio

362

$$364 \quad R(\omega) = \frac{S_{a,\text{self}}(\omega)}{S_{a,\text{th}}(\omega)} \quad (6)$$

363

365 provides a frequency-dependent measure of the margin to the thermal limit, where $S_{a,\text{th}}(\omega)$ denotes the thermal
366 noise contribution. Values of $R(\omega)$ close to unity indicate near-thermal-limited performance, whereas larger
367 values highlight the dominance of implementation-dependent noise sources.

368 This ratio constitutes a key diagnostic metric for sensor design, as it directly indicates whether further
369 performance improvements require fundamental changes to the mechanical plant or, alternatively,
370 technological improvements in readout, actuation, or digital acquisition. The interpretation of $R(\omega)$ across
371 frequency is illustrated in Fig. 4, where near-thermal and implementation-limited bands can be clearly
372 distinguished.

373 The spectral features identified in this section are a direct consequence of the causal structure of the digital
374 twin and the noise modeling assumptions introduced in Section 4. While the existence of plateaus and dominant
375 noise regimes is a robust qualitative result, their quantitative characteristics depend on model parameters and
376 uncertainty distributions.

377 Nonlinear effects, cross-correlations between noise sources, and non-stationary behaviour are not considered
378 in this analysis. These factors may alter the detailed spectral structure in real instruments, particularly under
379 extreme operating conditions. Nevertheless, the regime-based interpretation presented here provides a
380 physically meaningful and practically useful framework for guiding sensor design.

381

382

383 6. Crossover frequencies and design trade-offs

384 While the identification of dominant noise regimes provides a qualitative understanding of sensor performance,
385 practical design decisions require quantitative metrics capable of capturing transitions between regimes and
386 their dependence on key design parameters. In this section, such metrics are introduced through the concept of
387 crossover frequencies, which mark the boundaries between noise-dominated regimes and provide a compact
388 description of performance trade-offs.

389 A representative mapping of crossover frequencies and dominant regimes in the design parameter space is
390 shown in Fig. 6, which synthesises the spectral analyses discussed in the previous section.

391 For any pair of noise sources q_1 and q_2 , a crossover frequency $\omega_c^{(q_1, q_2)}$ is defined as the solution of

392

$$394 |T_{q_1}(\omega_c)|^2 S_{q_1}(\omega_c) = |T_{q_2}(\omega_c)|^2 S_{q_2}(\omega_c), \quad (7)$$

393

395 i.e. the frequency at which the contributions of the two noise sources to the total self-noise spectrum are equal.

396 Below and above this frequency, the dominant contribution switches from one noise source to the other.

397 In practice, the most relevant crossover frequencies involve transitions between thermal noise and
398 implementation-dependent noise sources, such as readout or digital acquisition noise. These transitions
399 delineate frequency intervals in which further performance improvements require fundamentally different
400 design strategies.

401 Building on the plateau definition introduced in Section 5, the near-plateau bandwidth is defined as the
402 frequency interval over which the self-noise remains within a prescribed margin of the minimum achievable
403 level. Formally, this interval is given by

404

$$406 N_a(\omega) \leq (1 + \delta) N_{a,\min}, \quad (8)$$

405

407 where $N_{a,\min}$ is the minimum value of the self-noise ASD and δ is a tolerance parameter. The near-plateau
408 bandwidth provides a concise metric for assessing the usable frequency range over which the sensor operates
409 close to its optimal sensitivity.

410 As illustrated in Fig. 6, this bandwidth is strongly dependent on implementation parameters such as ADC
411 resolution and control-loop design, and it often represents a more informative performance metric than the
412 absolute minimum noise level alone.

413 The crossover frequencies and near-plateau bandwidth jointly define a design trade-off space in which
414 improvements along one dimension may degrade performance along another. For example, increasing digital
415 resolution can extend the near-plateau bandwidth toward higher frequencies but may impose penalties in power
416 consumption or system complexity. Conversely, modifying mechanical damping may shift thermal-to-readout
417 crossover frequencies at the expense of increased sensitivity to environmental perturbations.

418 The regime maps shown in Fig. 6 summarise these trade-offs by identifying, for each region of the parameter
419 space, the noise source that ultimately limits performance. These maps constitute a consolidated result, as they
420 are derived directly from the noise-budget formalism and the causal structure of the digital twin. However, the
421 precise boundaries between regimes should be interpreted as model-dependent, reflecting assumptions on
422 parameter uncertainty and noise spectra.

423 From a design perspective, crossover-based metrics provide actionable guidance by indicating whether further
424 optimisation efforts should focus on fundamental mechanical improvements or on technological enhancements
425 in readout, actuation, or digital acquisition. In this sense, crossover frequencies act as decision thresholds
426 separating regimes where different design strategies are effective.

427 It is important to note that crossover frequencies are not intrinsic properties of the sensor but emerge from the
428 interaction between physical dynamics and implementation choices. As such, they should be interpreted within
429 the context of the assumed operating conditions and uncertainty model. The broader implications of this
430 dependence are discussed in Section 8.

431

432

433 **7. Performance metrics and design optimization**

434 The spectral analyses and crossover-based diagnostics introduced in the previous sections provide detailed
435 insight into the noise-limited behaviour of ultra-low-noise inertial sensors. For design purposes, however, it is
436 often desirable to condense this information into a limited set of performance metrics that can guide

437 optimisation decisions and enable comparisons between alternative architectures. This section introduces such
438 metrics and illustrates their role within the digital-twin framework.

439 A synthesis of the performance metrics discussed below and their dependence on key design parameters is
440 shown in Fig. 7, which summarises the design space explored in this study.

441 A primary metric is the minimum self-noise level, defined as

442

$$444 \quad N_{a,\min} = \min_{\omega} N_a(\omega), \quad (9)$$

443

445 where $N_a(\omega)$ is the self-noise ASD defined in Eq. (4). While $N_{a,\min}$ provides a compact measure of ultimate
446 sensitivity, it does not capture the frequency extent over which this sensitivity is achieved. As such, it should
447 not be used in isolation to rank sensor designs.

448 Complementary information is provided by the near-plateau bandwidth introduced in Section 6, which
449 quantifies the usable frequency interval over which the self-noise remains close to its minimum value.

450 Together, these two metrics define a sensitivity–bandwidth trade-off that is central to sensor design.

451 To assess how closely a given design approaches the fundamental thermal noise limit, the margin to the thermal
452 bound is evaluated using the ratio defined in Eq. (6). For practical design optimisation, a scalar metric can be
453 introduced by averaging this ratio over a frequency interval of interest $[\omega_1, \omega_2]$,

454

$$456 \quad \bar{R} = \frac{1}{\omega_2 - \omega_1} \int_{\omega_1}^{\omega_2} \frac{S_{a,\text{self}}(\omega)}{S_{a,\text{th}}(\omega)} d\omega. \quad (10)$$

455

457 Values of \bar{R} close to unity indicate near-thermal-limited performance over the selected band, whereas larger
458 values highlight the dominance of implementation-dependent noise sources. This metric is particularly useful
459 for identifying whether further optimisation efforts should focus on mechanical design or on technological
460 improvements in readout and digital acquisition.

461 Beyond absolute performance, robustness with respect to parameter uncertainty constitutes a critical aspect of
462 sensor design. Within the digital-twin framework, robustness is assessed by analysing the variability of the
463 performance metrics introduced above under the assumed parameter uncertainty distributions.
464 Designs that achieve marginally lower self-noise but exhibit strong sensitivity to parameter variations may be
465 less desirable than slightly noisier but more robust configurations. This consideration is especially relevant for
466 long-term geoscientific deployments, where environmental variability and ageing effects can significantly
467 impact performance (Wright and Davidson, 2024).
468 The optimisation strategy adopted here therefore prioritises uncertainty-aware performance, favouring regions
469 of the design space in which sensitivity, bandwidth, and robustness are jointly optimised. The regime maps
470 shown in Fig. 7 illustrate how such regions can be identified and compared across alternative design choices.
471 Within the proposed framework, design optimisation proceeds iteratively. Initial design choices define a
472 candidate digital twin, whose performance metrics are evaluated using the methods described above. Identified
473 bottlenecks then guide targeted modifications to mechanical parameters, control architecture, or digital
474 acquisition settings, and the analysis is repeated until the desired performance objectives are met.
475 This optimisation process is methodologically consolidated, as it relies on physically interpretable metrics
476 derived directly from the causal digital twin. At the same time, specific optimisation outcomes remain context-
477 dependent, reflecting application-specific requirements and constraints. The broader implications of this
478 balance between generality and specificity are discussed in Section 8.

479

480

481 **8. Discussion**

482 Recent advances in digital-twin methodologies for metrology have emphasised the importance of uncertainty
483 quantification, traceability, and physically consistent virtual experimentation (Wright and Davidson, 2024;
484 Maculotti et al., 2024). The present framework aligns with these developments by extending such principles
485 to force-feedback inertial sensors and explicitly incorporating causality constraints within the modeling
486 architecture.

487 This section discusses the implications of the proposed causal and uncertainty-aware digital-twin framework,
488 placing the results presented in Sections 4–7 in a broader methodological and instrumental context. The

489 discussion focuses on the generality of the approach, its limitations, and its relevance for the design of ultra-
490 low-noise geoscientific inertial sensors.

491 A conceptual synthesis of the workflow and its role in guiding design decisions is illustrated in Fig. 8, which
492 integrates the individual analysis steps into a unified methodological framework.

493 A key outcome of this study is that enforcing physical causality and realisability constraints at the digital-twin
494 level is essential for obtaining meaningful metrological predictions. Non-causal or idealised representations
495 may lead to overly optimistic noise estimates and obscure the distinction between fundamental and
496 implementation-dependent limits. (Wright and Davidson, 2024; Maculotti et al., 2024).

497 The practical relevance of these metrics can be illustrated through representative design scenarios based on
498 Figs. 4–7.

499 In a first scenario, consider a design operating close to the thermal noise limit over a restricted frequency band,
500 as indicated by $R(\omega) \approx 1$ in Fig. 4. In this regime, further improvements in sensitivity cannot be achieved
501 through readout or digital optimisation alone, and require modifications of the mechanical plant, such as
502 reducing dissipation or increasing effective mass. This identifies the thermal-to-readout crossover as a key
503 decision threshold between mechanical and electronic optimisation strategies.

504 In a second scenario, Fig. 6 shows that increasing ADC resolution shifts the crossover between digital and
505 actuation noise toward higher frequencies, effectively extending the near-plateau bandwidth. However, as
506 illustrated in Fig. 7, this improvement saturates beyond a certain ENOB (Effective Number of Bits), beyond
507 which actuator or readout noise becomes dominant. This demonstrates that digital optimisation alone cannot
508 ensure broadband performance gains.

509 A third scenario concerns the role of damping, as shown in Fig. 5. Variations in damping primarily affect low-
510 frequency performance through their impact on thermal noise and feedback dynamics, while high-frequency
511 behaviour remains largely unchanged. This indicates that mechanical and digital parameters act on distinct
512 spectral regions, enabling targeted and decoupled optimisation strategies.

513 The performance metrics introduced in Sections 6 and 7 provide a compact representation of complex spectral
514 information and facilitate comparison between alternative sensor architectures. In particular, crossover
515 frequencies and near-plateau bandwidths offer actionable indicators of where design effort is most effectively
516 directed.

517 The proposed framework can be further contextualised by comparison with conventional sensor design
518 methodologies. Traditional noise budgeting approaches typically evaluate individual noise contributions
519 independently and combine them a posteriori, often neglecting system-level coupling effects introduced by
520 feedback control and digital acquisition. While such approaches are effective for first-order performance
521 estimation, they may lead to inconsistencies when applied to closed-loop architectures, where transfer
522 functions are inherently interdependent.

523 Simplified digital twin models, on the other hand, often represent individual subsystems or rely on non-causal
524 inversions to estimate idealised performance limits. Although computationally efficient, these formulations
525 may overlook constraints imposed by causality and realisability, leading to optimistic predictions of achievable
526 sensitivity.

527 In contrast, the present framework enforces causal system dynamics at all stages and propagates all noise
528 sources through a unified set of transfer functions, enabling a consistent system-level evaluation. The resulting
529 performance metrics, including crossover frequencies (Eq. 7) and near-plateau bandwidth (Eq. 8), provide
530 quantitative indicators that are not directly accessible through conventional noise budgeting approaches.

531 From a quantitative perspective, the ratio to the thermal limit (Eq. 6) and its band-averaged form (Eq. 10)
532 enable a direct comparison between designs, while explicitly accounting for implementation-dependent
533 constraints. These metrics highlight how different design strategies shift regime boundaries rather than
534 uniformly improving performance, an effect that is not captured by traditional component-wise optimisation.

535 This comparison indicates that the main advantage of the proposed digital twin lies not in redefining
536 fundamental limits, but in providing a physically consistent and uncertainty-aware framework to approach
537 them in a controlled and interpretable manner.

538 A schematic comparison of the different methodological approaches is provided in Fig. 9, highlighting how
539 the proposed framework enables physically consistent and uncertainty-aware system-level design.

540 The regime maps derived from these metrics should be interpreted as decision-support tools rather than as
541 absolute performance predictors. While the existence of distinct noise-dominated regimes is a robust outcome
542 of the noise-budget formalism, the precise boundaries between regimes depend on modelling assumptions and
543 uncertainty characterisation. This sensitivity underscores the importance of uncertainty-aware optimisation
544 strategies in sensor design.

545 Although the digital twin is formulated with force-feedback inertial sensors in mind, the underlying
546 methodology is not restricted to a specific sensor type. The same framework can be adapted to other classes of
547 geoscientific instruments, such as tiltmeters, gravimeters, or strain sensors, including atom-interferometry
548 gravimeters demonstrated in harsh volcanic environments (Antoni-Micollier et al., 2022), provided that their
549 dynamics can be represented within a linear, causal system framework.

550 The abstraction of transduction, actuation, and digital acquisition as modular subsystems facilitates such
551 extensions and supports the development of sensor-specific digital twins within a common metrological
552 structure. This generality is consistent with recent efforts to standardise digital-twin methodologies across
553 measurement domains (Ríos et al., 2020; Ubezio et al., 2023).

554 Several limitations of the present framework should be acknowledged. First, the analysis assumes linearity,
555 stationarity, and mutual incoherence of noise sources. While these assumptions are standard in inertial sensor
556 metrology, they may be violated under extreme operating conditions or in the presence of strong environmental
557 coupling.

558 Second, parameter uncertainties are treated as statistically independent unless explicitly stated. In real
559 instruments, correlations between mechanical, electronic, and environmental parameters may exist and could
560 affect uncertainty propagation. Incorporating such correlations would require additional modelling effort and
561 data, which lies beyond the scope of the present study.

562 Finally, the framework does not incorporate site-specific noise conditions or experimental calibration data. As
563 a result, the predicted performance should be interpreted as an intrinsic sensor capability rather than as a
564 guarantee of field performance. This distinction is particularly important when comparing digital-twin
565 predictions with observational data.

566 A further limitation of the present study is the lack of direct experimental validation against specific sensor
567 prototypes. This reflects the intended role of the proposed digital twin as a design-stage and feasibility-
568 assessment tool, rather than as a post-deployment calibration framework.

569 In this context, the objective is not to reproduce the performance of a particular instrument, but to provide a
570 physically consistent and causality-constrained environment for exploring design trade-offs and identifying
571 fundamental and implementation-dependent performance limits.

572 Nevertheless, the integration of the digital twin with experimental data represents a natural and important
573 extension of the present work, as demonstrated by recent metrology-integrated digital twin frameworks that
574 explicitly combine physical models with measurement data for validation and calibration purposes (Samadi et
575 al., 2025). Future developments may include the use of laboratory or field measurements to calibrate model
576 parameters, validate predicted self-noise spectra, and refine uncertainty distributions within a data-informed
577 framework.

578 Despite these limitations, the proposed framework provides a solid foundation for future extensions. Potential
579 developments include the incorporation of nonlinear effects, the integration of experimental calibration data
580 to refine parameter distributions, and the coupling of the digital twin with real-time monitoring systems. Data-
581 driven denoising approaches have also been explored for inertial sensors/accelerometers and may complement
582 model-based digital twins (Yang et al., 2023).

583 Such extensions would further enhance the utility of digital twins as tools for both design-stage optimisation
584 and operational performance assessment in geoscientific instrumentation.

585

586

587 **9. Conclusions**

588 This work introduces a causal and uncertainty-aware digital-twin framework for the design and metrological
589 assessment of ultra-low-noise geoscientific inertial sensors. The framework integrates mechanical dynamics,
590 force-feedback control, transduction, and digital acquisition within a physically realisable and causally
591 consistent representation.

592 A central contribution is the formulation of a unified noise-budget model that distinguishes between
593 fundamental thermal limits and implementation-dependent noise sources, enabling physically interpretable
594 self-noise predictions and uncertainty-aware performance assessment.

595 The results demonstrate that enforcing causality and realisability is essential for obtaining reliable performance
596 estimates, particularly in ultra-low-noise regimes where idealised formulations may lead to overly optimistic
597 predictions.

598 Despite the simplifying assumptions adopted, the proposed framework provides a robust and extensible
599 foundation for design-stage optimisation and virtual experimentation. Potential extensions include the
600 incorporation of nonlinear effects, correlated uncertainties, and experimental calibration data.

601 Beyond inertial sensors, the methodology is readily transferable to other classes of geoscientific instruments,
602 supporting the broader adoption of digital twins as design and decision-support tools in geoscientific
603 instrumentation.

604

605

606 **Competing interests:**

607 The authors declare that they have no conflict of interest

608

609

610 **10. References**

611 Antoni-Micollier, L., *et al.* (2022). Detecting volcano-related underground mass changes with a quantum
612 gravimeter. *Geophysical Research Letters*, 49, e2022GL097814. <https://doi.org/10.1029/2022GL097814>

613

614 Bai, W., Feng, W., Wang, P., Zhang, Z., and Zhao, G. (2025). Research on Interferometric Tilt Sensor for
615 Vibration Isolation Platform. *Sensors*, 25(6), 1777. <https://doi.org/10.3390/s25061777>

616

617 *Bendat, J. S., & Piersol, A. G. (2010). Random Data: Analysis and Measurement Procedures (4th ed.). Wiley.*

618 <https://doi.org/10.1002/9781118032428>

619

620 Brown, D. D., Jones, P., Rowlinson, S., Leavey, S., Green, A. C., Töyrä, D., and Freise, A. (2020). Pykat:
621 Python package for modelling precision optical interferometers. *SoftwareX*, 12, 100613.
622 <https://doi.org/10.1016/j.softx.2020.100613>

623

624 Carlin, *et al.* (2024). An interactive framework to support decision-making for Digital Twin design. *Journal of*
625 *Industrial Information Integration*, 41, 100639. <https://doi.org/10.1016/j.jii.2024.100639>

626

627 Carter, J. J., Birckigt, P., Gerberding, O., and Koehlenbeck, S. M. (2024). High precision inertial sensors on a
628 one inch diameter optic. *Scientific Reports*, 14. <https://doi.org/10.1038/s41598-024-68623-0>

629

630 Carter, J. J., *et al.* (2025). Testing compact, fused silica resonator based inertial sensors in a gravitational wave
631 detector prototype facility. *Classical and Quantum Gravity*, 42(18), 185001. [https://doi.org/10.1088/1361-](https://doi.org/10.1088/1361-6382/adff34)
632 [6382/adff34](https://doi.org/10.1088/1361-6382/adff34)

633

634 **Chen, Y., Liu, X., Wang, L., Yu, T., Wang, Z., Xue, K., Sui, Y., & Chen, Y. (2024). Research and optimization**
635 **of high-performance front-end circuit noise for inertial sensors. *Sensors*, 24(3), 805.**
636 **<https://doi.org/10.3390/s24030805>**

637

638 Collette, C., Janssens, S., Fernandez-Carmona, P., Artoos, K., Guinchard, M., Hauviller, C., and Preumont, A.
639 (2012). Review: Inertial sensors for low-frequency seismic vibration measurement. *Bulletin of the*
640 *Seismological Society of America*, 102(4), 1289–1300. <https://doi.org/10.1785/0120110223>

641

642 El-Sheimy, N., Yoon, S., and Jiang, Z. (2020). Inertial sensors technologies and error modelling for navigation
643 and uncertainty analysis. *Journal of Applied Geodesy*, 14(2), 115–134. [https://doi.org/10.1186/s43020-019-](https://doi.org/10.1186/s43020-019-0001-5)
644 [0001-5](https://doi.org/10.1186/s43020-019-0001-5)

645

646 Kranzhoff, S. L., Lehmann, J., Kirchhoff, R., *et al.* (2023). A vertical inertial sensor with interferometric
647 readout. *Classical and Quantum Gravity*, 40(1), 015007. <https://doi.org/10.1088/1361-6382/aca45b>

648

649 Maculotti, G., Elster, C., Wübbeler, G., *et al.* (2024). A shared metrological framework for trustworthy virtual
650 experiments and digital twins. *Metrology*, 4(3), 337–363. <https://doi.org/10.3390/metrology4030021>

651

652 Mitchell, A., *et al.* (2025). Integration of high-performance compact interferometric sensors in a suspended
653 interferometer. *Classical and Quantum Gravity*, 42(19), 195014. <https://doi.org/10.1088/1361-6382/ae0087>
654

655 Oppenheim, A. V., & Schaffer, R. W. (2010). *Discrete-Time Signal Processing* (3rd ed.)
656 Prentice Hall. ISBN: 9780131988424
657

658 Poroskun, I., Rothleitner, C., and Heißelmann, D. (2022). Structure of digital metrological twins as software
659 for uncertainty estimation. *Journal of Sensors and Sensor Systems*, 11, 75–82. [https://doi.org/10.5194/jsss-11-](https://doi.org/10.5194/jsss-11-75-2022)
660 [75-2022](https://doi.org/10.5194/jsss-11-75-2022)
661

662 Prasad, A., Middlemiss, R. P., Noack, A., *et al.* (2022). A 19 day earth tide measurement with a MEMS
663 gravimeter. *Scientific Reports*, 12, 13091. <https://doi.org/10.1038/s41598-022-16881-1>
664

665 Ríos, J., Staudter, G., Weber, M., and Anderl, R. (2020). Uncertainty of data and the digital twin: a review.
666 *International Journal of Product Lifecycle Management*, 12(4), 329–358.
667 <https://doi.org/10.1504/IJPLM.2020.10035102>
668

669 Samadi, H., Ahsan, M. M., & Raman, S. (2025). Metrology and manufacturing-integrated digital twin (MM-
670 DT) for advanced manufacturing: Insights from coordinate measuring machine (CMM) and FARO arm
671 measurements. *Next Research*, 2(2), 100299. <https://doi.org/10.1016/j.nexres.2025.100299>
672

673 Sepahi-Boroujeni, S., & Khameneifar, F. (2024). Digital twin-enabled error and uncertainty mapping for 3D
674 scanning. *Precision Engineering*. <https://doi.org/10.1016/j.precisioneng.2024.03.007>
675

676 Scholz, G., Fortmeier, I., Marschall, M., *et al.* (2022). Experimental design for virtual experiments in tilted-
677 wave interferometry. *Metrology*, 2(1), 84–97. <https://doi.org/10.3390/metrology2010006>
678

679 Sider, A., Di Fronzo, C., Amez-Droz, L., *et al.* (2023). E-TEST: a compact low-frequency isolator for a large
680 cryogenic mirror. *Classical and Quantum Gravity*, 40(16), 165002. <https://doi.org/10.1088/1361-6382/ace230>
681

682 Sun, Z., Wang, Q., Pan, J., *et al.* (2024). Review on digital twin applications and development challenges in
683 structural monitoring. *Sensors*, 25(1), 59. <https://doi.org/10.3390/s25010059>
684

685 Ubezio, B., Ergun, S., and Zangl, H. (2023). Realistic sensor simulations for the digital twin.
686 *e+i Elektrotechnik und Informationstechnik*, 140(10), 562–571. <https://doi.org/10.1007/s00502-023-01156-y>
687

688 Ubhi, A. S., Prokhorov, L., Cooper, S., *et al.* (2022). Active platform stabilization with a 6D seismometer.
689 *Applied Physics Letters*, 121, 174101. <https://doi.org/10.1063/5.0118606>
690

691 van Dongen, J., *et al.* (2023). Reducing control noise in gravitational wave detectors with interferometric local
692 damping of suspended optics. *Review of Scientific Instruments*, 94(5), 054501.
693 <https://doi.org/10.1063/5.0144865>
694

695 Vlaeyen, M., *et al.* (2021). Digital twin of an optical measurement system.
696 *Sensors*, 21(19), 6638. <https://doi.org/10.3390/s21196638>
697

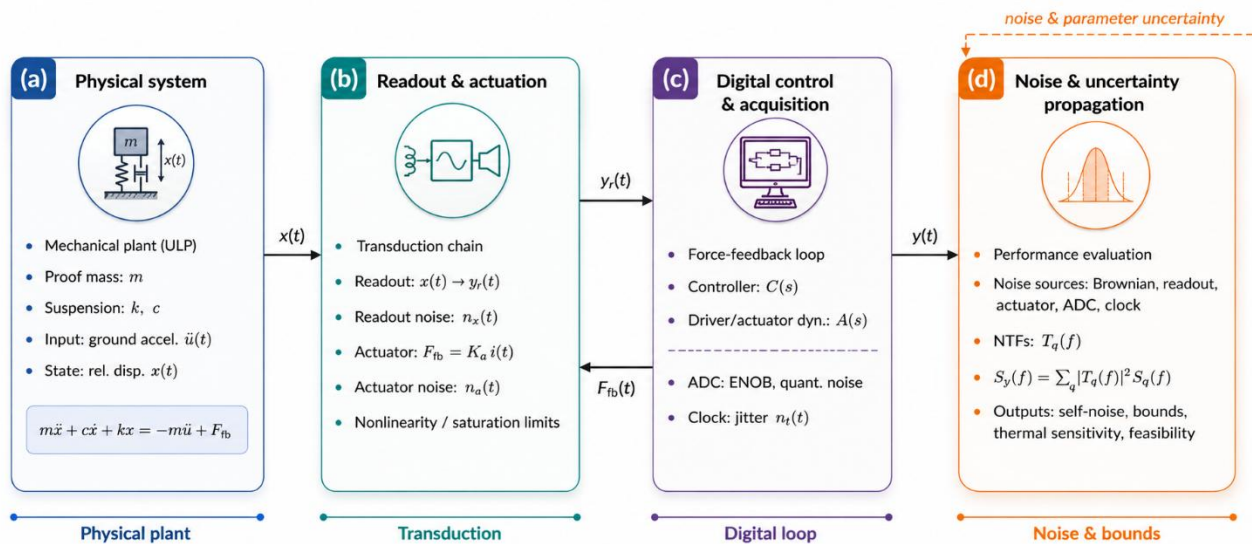
698 Wright, L., and Davidson, S. (2024). Digital twins for metrology; metrology for digital twins.
699 *Measurement Science and Technology*, 35. <https://doi.org/10.1088/1361-6501/ad2050>
700

701 Wübbeler, G., Marschall, M., Kniel, K., Heißelmann, D., Härtig, F., and Elster, C. (2022). GUM-Compliant
702 Uncertainty Evaluation Using Virtual Experiments. *Metrology*, 2(1), 114–127.
703 <https://doi.org/10.3390/metrology201000>
704

705 Zhao, G., *et al.* (2022). An interferometric inertial sensor for low-frequency seismic isolation.
706 *Sensors and Actuators A: Physical*, 335, 113398. <https://doi.org/10.1016/j.sna.2022.113398>

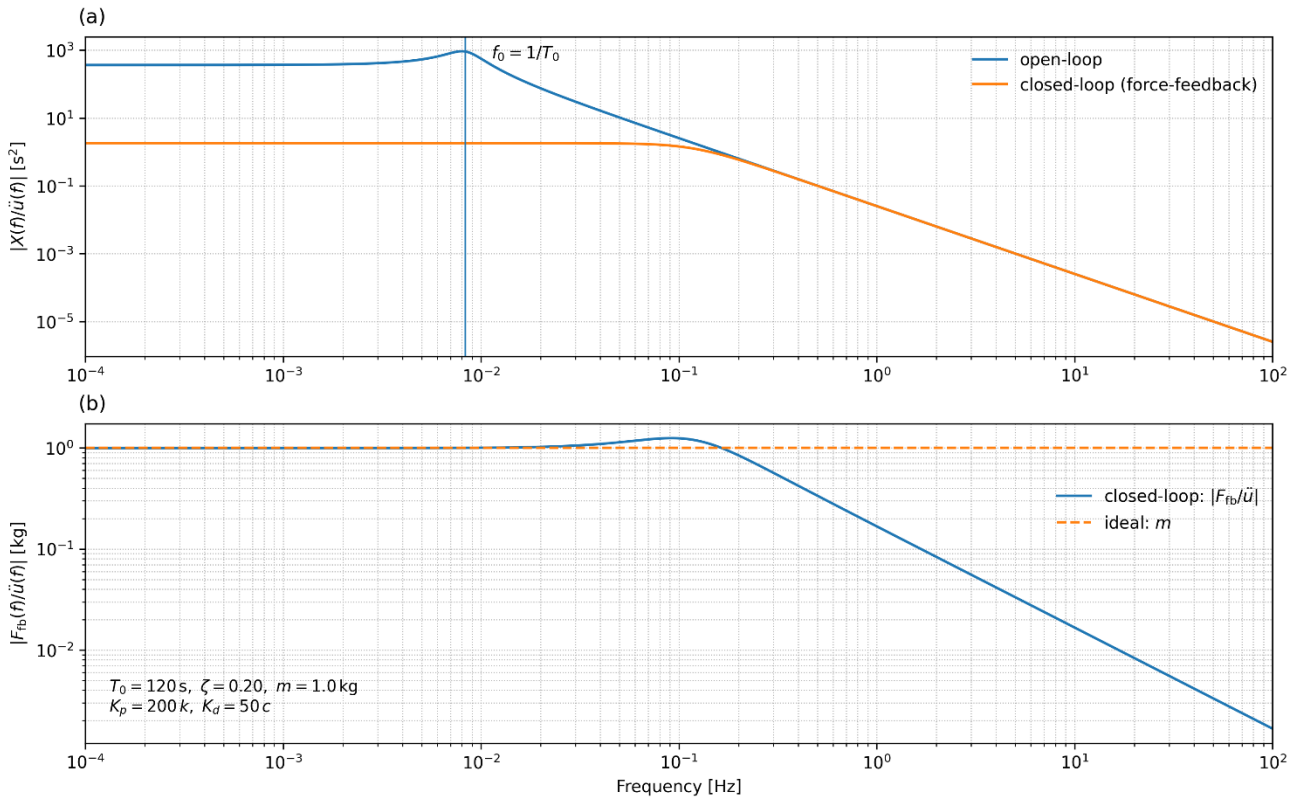
707

708 Yang, Z., Zhang, H., Xu, P., and Luo, Z. (2023). Unsupervised Noise Reductions for Gravitational Reference
709 Sensors or Accelerometers Based on the Noise2Noise Method. *Sensors*, 23(13), 6030.
710 <https://doi.org/10.3390/s23136030>



711

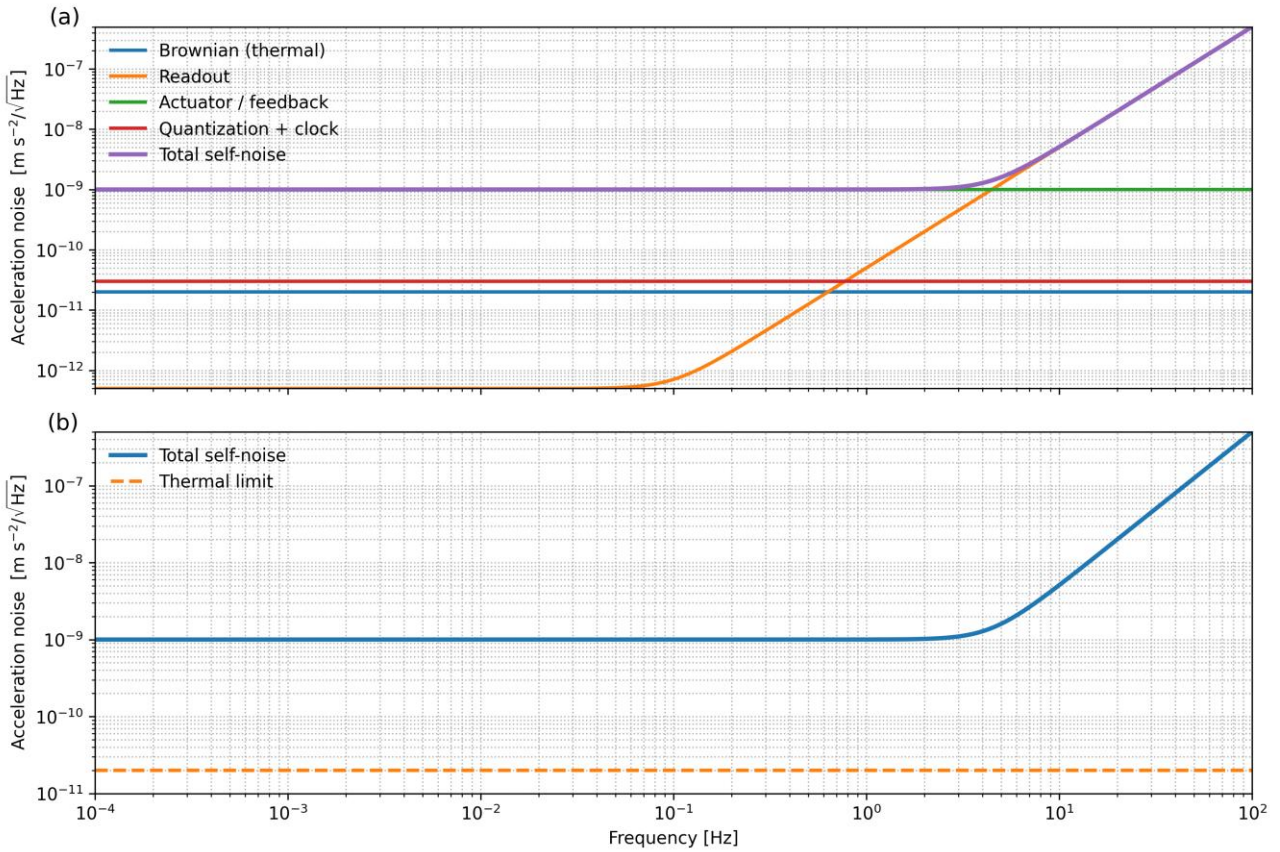
712 **Figure 1.** Conceptual block diagram of the digital-twin framework adopted for the analysis and design of a
 713 force-feedback ultra-long-period (ULP) seismometer. (a) Physical system: mechanical plant modeled as a
 714 proof mass–spring–damper system, driven by ground acceleration and controlled via feedback force, described
 715 by the equation of motion $m\ddot{x} + c\dot{x} + kx = -m\ddot{u} + F_{fb}$. (b) Readout and actuation: transduction chain
 716 mapping the relative displacement $x(t)$ into the readout signal $y_r(t)$, including readout noise and actuator
 717 dynamics, force generation, and nonlinearity or saturation effects. (c) Digital control and acquisition: closed-
 718 loop force-feedback architecture comprising the digital controller $C(s)$, driver/actuator dynamics $A(s)$,
 719 analog-to-digital conversion (ENOB and quantization noise), and clock jitter, yielding the output signal $y(t)$ in
 720 physical units. (d) Noise and uncertainty propagation: evaluation of the contribution of independent noise
 721 sources (Brownian, readout, actuator, ADC, and clock) through their corresponding noise transfer functions
 722 $T_q(f)$, resulting in the output power spectral density $S_y(f) = \sum_q |T_q(f)|^2 S_q(f)$. The framework enables
 723 quantitative assessment of self-noise, theoretical performance bounds, thermal sensitivity, and overall
 724 feasibility of the instrument design.



725

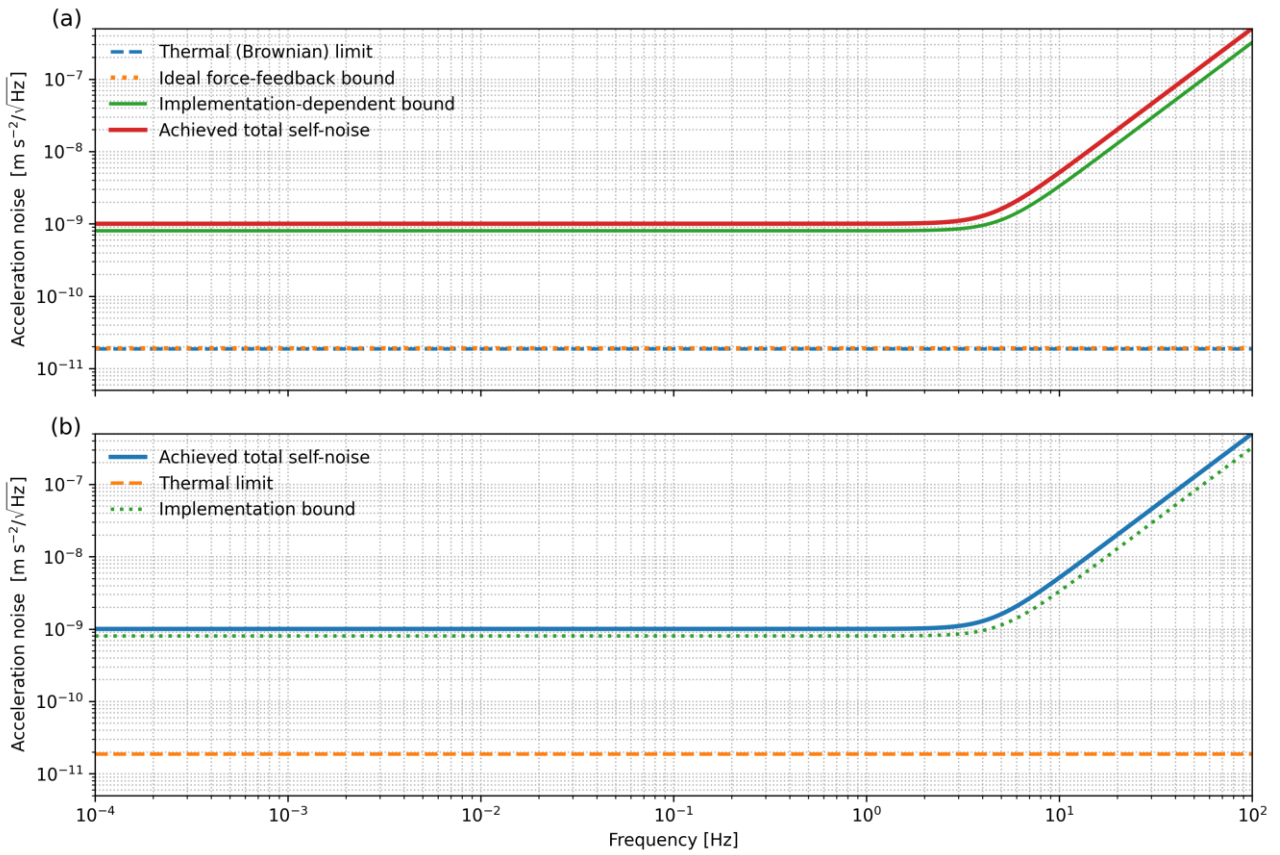
726 **Figure 2.** Frequency-domain response of the ultra-long-period (ULP) force-feedback seismometer digital twin.

727 (a) Magnitude of the mechanical compliance $|X(f)/\ddot{u}(f)|$, comparing the open-loop response of the
 728 mechanical plant with the closed-loop response obtained through force-feedback control. The open-loop
 729 resonance at the natural frequency $f_0 = 1/T_0$ is clearly visible, while the closed-loop configuration suppresses
 730 the resonance and significantly reduces proof-mass motion over a broad frequency band. (b) Magnitude of the
 731 force-balance transfer function $|F_{fb}(f)/\ddot{u}(f)|$ in the closed-loop configuration, compared with the ideal low-
 732 frequency limit $F_{fb}/\ddot{u} = m$. At low frequencies, the feedback force accurately tracks the inertial force
 733 associated with ground acceleration, whereas at higher frequencies the response rolls off due to the finite
 734 bandwidth of the control loop. The parameters reported in the inset correspond to a representative ULP
 735 configuration and a proportional–derivative feedback law.



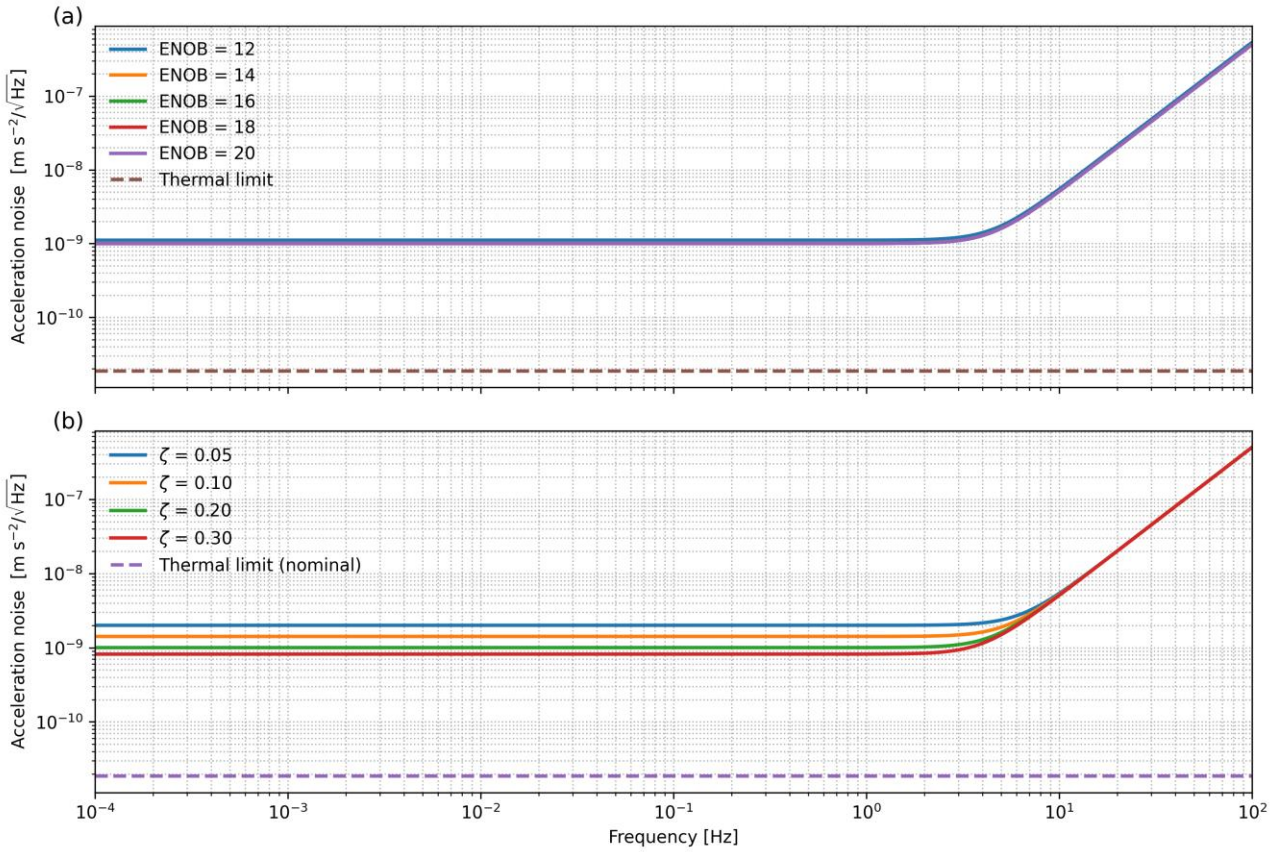
736

737 **Figure 3.** Frequency-dependent acceleration self-noise budget of the force-feedback ULP seismometer derived
 738 from the digital-twin framework. (a) Individual noise contributions referred to input acceleration, including
 739 Brownian (thermal) noise of the mechanical plant, readout noise, actuator/feedback noise, and quantization
 740 plus clock jitter, together with their quadratic sum defining the total self-noise. The spectrum highlights the
 741 transition from readout- and quantization-limited performance at low frequencies to feedback- and control-
 742 limited behavior at higher frequencies. (b) Comparison between the total self-noise and the fundamental
 743 thermal limit set by the mechanical suspension. Model parameters are indicated in the panel and correspond
 744 to a nominal ultra-long-period design with force-feedback control. The separation between the total self-noise
 745 and the thermal limit quantifies the residual performance gap attributable to non-thermal noise sources and
 746 control-loop implementation.



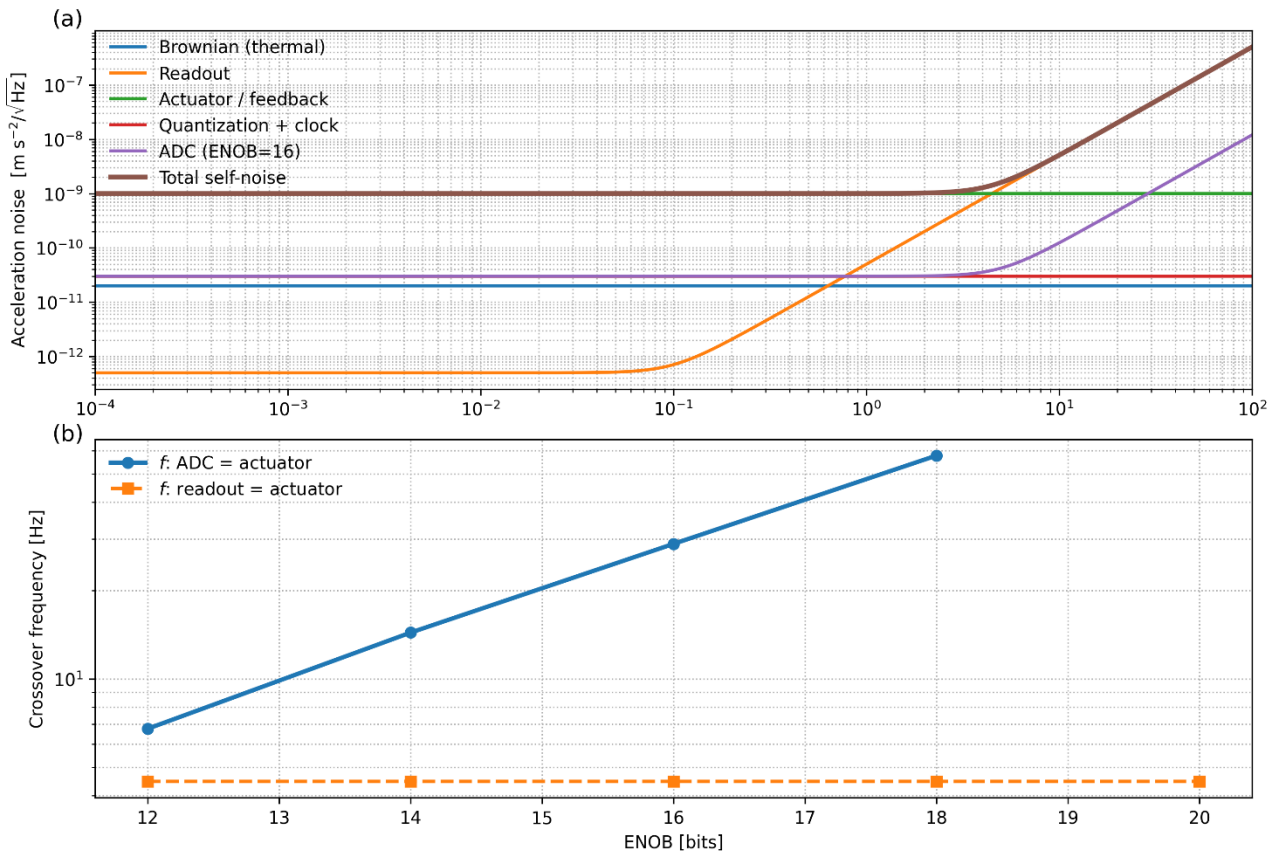
747

748 **Figure 4.** Metrological acceleration-noise bounds and achieved performance of the force-feedback ultra-long-
 749 period (ULP) seismometer derived from the digital-twin framework. (a) Fundamental and implementation-
 750 dependent noise bounds referred to input acceleration. The thermal (Brownian) limit represents the irreducible
 751 noise floor imposed by mechanical dissipation in the suspension. The ideal force-feedback bound coincides
 752 with the thermal limit in the absence of electronic and control noise and is shown with a slight offset for visual
 753 clarity. The implementation-dependent bound accounts for practical non-idealities introduced by actuation,
 754 digitization, timing, and control-loop dynamics, and exhibits a frequency-dependent rise imposed by closed-
 755 loop causality. The achieved total self-noise is shown for reference. (b) Comparison between the achieved total
 756 self-noise and the theoretical bounds. The separation from the thermal limit quantifies the residual
 757 performance gap attributable to control-loop implementation and electronic noise sources, providing a direct
 758 metric to assess design margins and guide further optimization toward fundamental physical limits.



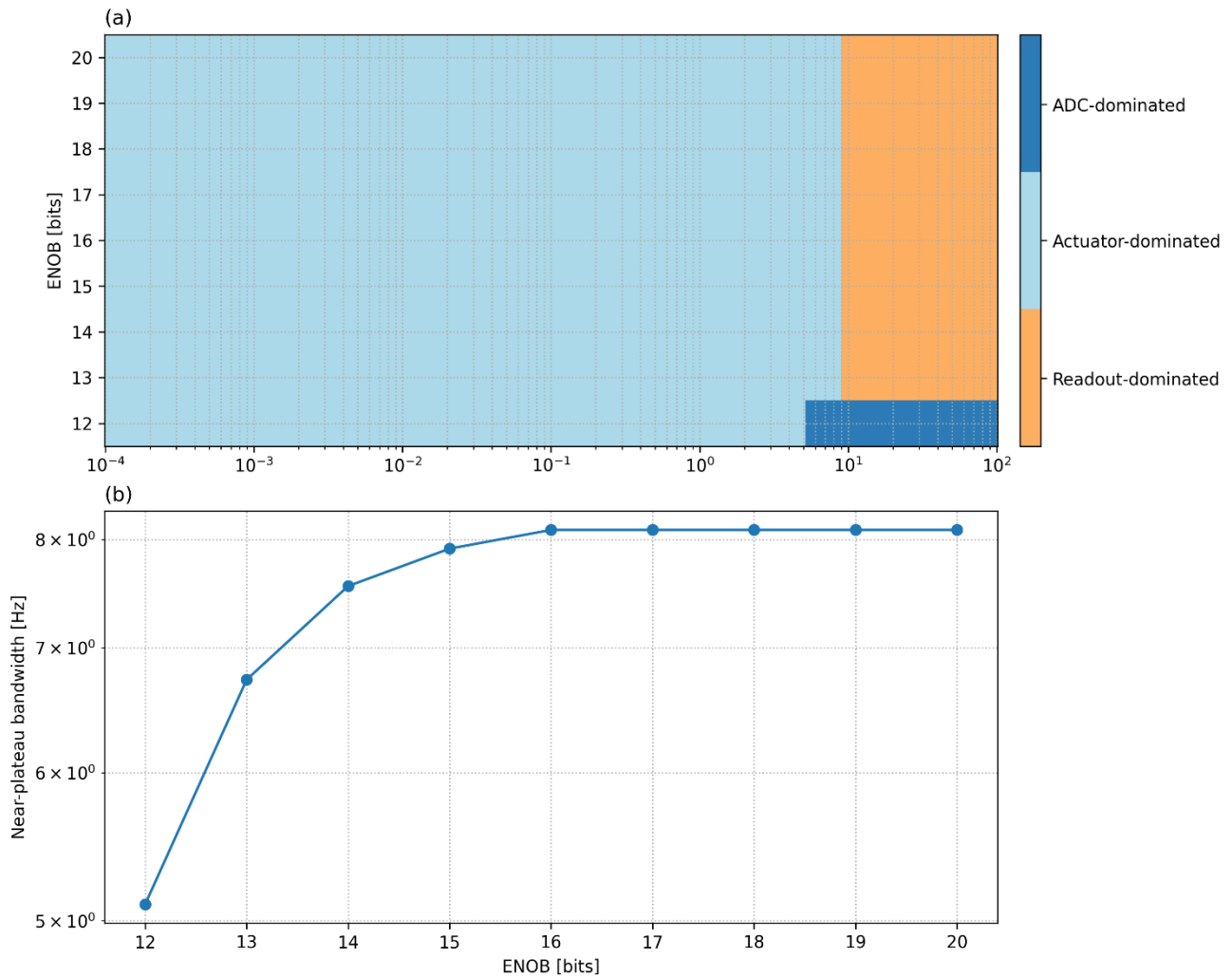
759

760 **Figure 5.** Spectral sensitivity of the closed-loop instrument self-noise to key design parameters. (a) Total
 761 acceleration self-noise amplitude spectral density $S_a^{1/2}(f)$ for different effective ADC resolutions (ENOB =
 762 12–20 bits), computed for a fixed mechanical plant ($m = 1$ kg, $T_0 = 120$ s, $\zeta = 0.20$) and identical control
 763 architecture. At low frequencies the spectra collapse onto a common plateau set by non-digital noise sources,
 764 whereas at higher frequencies the achievable noise floor progressively improves with increasing ENOB as
 765 quantization and digital-chain contributions are reduced. The dashed curve indicates the Brownian (thermal)
 766 acceleration limit, shown for reference. (b) Sensitivity of the total acceleration self-noise to the damping ratio
 767 ζ (0.05–0.30) at fixed ENOB (16 bits). Variations in ζ primarily affect the low-frequency noise level through the
 768 balance between thermal dissipation and feedback-related contributions, while the high-frequency rise
 769 remains controlled by the digital and readout bandwidth. The dashed line marks the nominal thermal limit.
 770 Together, the two panels illustrate how electronic resolution and mechanical damping act on distinct frequency
 771 regimes, defining complementary design trade-offs for ultra-low-frequency force-feedback inertial sensors.



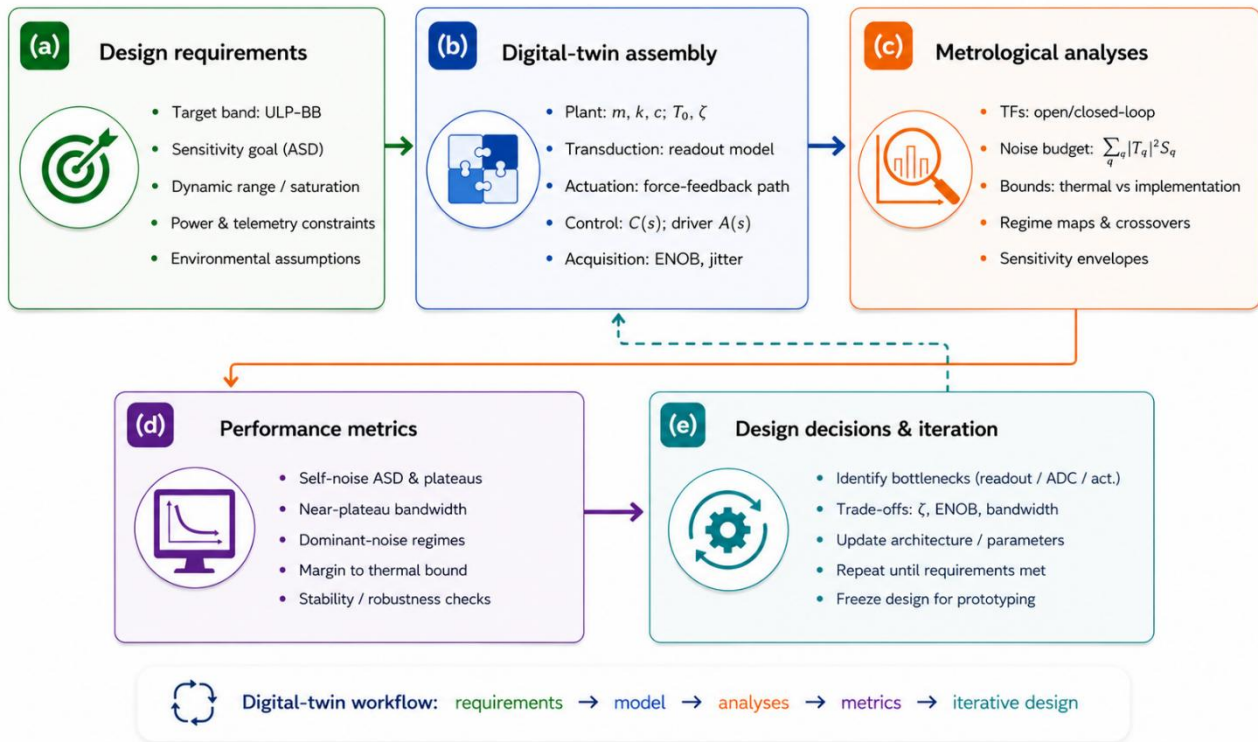
772

773 **Figure 6.** Noise regimes and crossover frequencies in a digitally controlled broadband inertial sensor. (a)
 774 Acceleration noise amplitude spectral density (ASD) as a function of frequency, showing the individual
 775 contributions from Brownian (thermal) noise, readout noise, actuator/feedback noise, quantization and clock
 776 noise, and the digital (ADC) contribution for a nominal resolution of ENOB = 16 bits. The resulting total self-
 777 noise (quadratic sum of all components) is also shown. The plot highlights the frequency-dependent dominance
 778 of different noise sources, with readout noise governing the low-frequency range, actuator/feedback noise
 779 setting the mid-band floor, and digital/ADC-related effects becoming relevant at higher frequencies due to
 780 closed-loop shaping. (b) Crossover frequencies between selected noise contributions as a function of effective
 781 ADC resolution (ENOB). The blue curve indicates the frequency at which ADC noise equals actuator/feedback
 782 noise, demonstrating the systematic extension of the near-thermal bandwidth with increasing ENOB. The
 783 orange curve shows the crossover between readout and actuator noise, which remains nearly invariant with
 784 ENOB, reflecting its weak dependence on digitization resolution. Together, panels (a) and (b) illustrate how
 785 digital resolution primarily controls the high-frequency noise budget, while low- and mid-band performance
 786 are constrained by analog sensing and actuation mechanisms.



787

























788 **Figure 7.** Design regime map and effective near-plateau bandwidth. (a) Dominant self-noise contributor in
 789 the ENOB–frequency plane, classified by variance comparison between readout, actuator/feedback, and ADC
 790 noise terms. The map highlights distinct operating regimes and shows that, for typical design parameters, the
 791 system is predominantly actuator-limited over most of the seismic bandwidth, with ADC-dominated behavior
 792 confined to low ENOB and high frequencies, and readout domination emerging at the highest frequencies. (b)
 793 Near-plateau bandwidth as a function of ENOB, defined as the frequency range over which the total self-noise
 794 remains within 30% of its minimum achievable plateau. Increasing ENOB significantly extends the usable low-
 795 noise bandwidth up to $ENOB \approx 15\text{--}16$, beyond which further improvements yield diminishing returns,
 796 indicating a transition to actuator/readout-limited performance. This representation provides a compact and
 797 quantitative guideline for digitization requirements in force-feedback broadband sensors.




798

799 **Figure 8.** Conceptual workflow of the digital-twin framework adopted for the engineering design and
 800 metrological assessment of ultra-low-noise broadband inertial sensors. (a) Definition of design requirements,
 801 including target bandwidth, sensitivity objectives, dynamic range constraints, and environmental assumptions.
 802 (b) Assembly of the digital twin, integrating the mechanical plant, transduction chain, force-feedback
 803 actuation, control architecture, and acquisition system. (c) Metrological analyses performed in the frequency
 804 domain, encompassing open- and closed-loop transfer functions, full noise-budget decomposition, and
 805 theoretical versus implementation-dependent performance bounds. (d) Extraction of performance metrics,
 806 such as self-noise plateaus, near-plateau bandwidth, dominant noise regimes, and margins relative to the
 807 thermal limit. (e) Iterative design loop, where identified bottlenecks guide trade-offs among damping, ENOB,
 808 and bandwidth, leading to progressive architectural refinement and final design freeze. Solid arrows indicate
 809 the nominal forward workflow, whereas the dashed arrow highlights the feedback loop driving iterative
 810 optimization.

811

| | Traditional Noise Budgeting <i>Component-wise approach</i> | Simplified Digital Twin Models <i>Subsystem-based or non-causal</i> | Proposed Framework <i>Causal and Uncertainty-Aware Digital Twin</i> |
|---|---|--|---|
|  Physical causality |  Not explicitly enforced Assumes ideal transformations and post-processing inversions. |  Partially enforced or neglected Often relies on idealized or non-causal inversions. |  Explicitly enforced All transformations are causal and physically realizable. |
|  System-level coupling |  Neglected or approximated Interactions between mechanical, electrical, and digital domains are not fully captured. |  Subsystem-based Models individual blocks; weak representation of cross-domain coupling and feedback. |  Fully integrated Mechanical, electrical, and digital domains are coupled through closed-loop dynamics. |
|  Uncertainty propagation |  Limited Uncertainties treated independently for each component; correlations typically ignored. |  Limited or qualitative Uncertainty usually assessed qualitatively or with simplified assumptions. |  Systematic and distribution-based Uncertainty propagated through all transfer functions using Monte Carlo analysis. |
|  Noise modeling consistency |  Additive and a posteriori Noise contributions added after independent evaluation of subsystems. |  May include idealizations Noise modeled with simplifications; non-causal operations may be introduced. |  Fully consistent All noise sources mapped through their physical transfer functions in a unified framework. |
|  Performance metrics |  Component-level only Provides individual noise floors but no system-level metrics such as crossover frequencies. |  Limited system-level metrics Provides global sensitivity estimates but typically lacks bandwidth-related metrics. |  Advanced system-level metrics <ul style="list-style-type: none"> • Crossover frequencies (Eq. 7) • Near-plateau bandwidth (Eq. 8) • Thermal ratio metrics (Eq. 6, 10) |
|  Typical limitations |  Ignores feedback coupling and closed-loop effects May lead to inconsistent or non-realizable performance predictions. |  Can lead to optimistic performance predictions Non-causal modeling may violate realizability and physical constraints. |  Increased model complexity Requires accurate parameterization and computational resources. |

Increasing physical consistency and predictive capability 

812

813 **Figure 9.** Comparative assessment of sensor design methodologies for ultra-low-noise inertial systems. The
814 diagram contrasts traditional noise budgeting, simplified digital twin approaches, and the proposed causal
815 and uncertainty-aware digital-twin framework in terms of physical causality, system-level coupling,
816 uncertainty propagation, noise modeling consistency, and performance metrics. Conventional approaches
817 either neglect feedback-induced coupling or rely on simplified or non-causal representations, limiting their
818 ability to provide consistent system-level predictions. In contrast, the proposed framework enforces causal
819 dynamics and propagates all noise sources through a unified transfer-function representation, enabling
820 physically consistent evaluation and the definition of advanced performance metrics such as crossover
821 frequencies and near-plateau bandwidth.